ACS MATERIALS LETTERS

www.acsmaterialsletters.org

LETTER

Robust Barium Phosphonate Metal–Organic Frameworks Synthesized under Aqueous Conditions

Khalifah A. Salmeia,* Simone Dolabella,‡ Dambarudhar Parida,‡ Terry J. Frankcombe, Akef T. Afaneh, Kyle E. Cordova, Bassem Al-Maythalony, Shanyu Zhao, Romain Civioc, Ali Marashdeh, Bernhard Spingler, Ruggero Frison, and Antonia Neels*

Cite This: *ACS Materials Lett.* 2021, 3, 1010–1015

Read Online

ACCESS | Metrics & More | Article Recommendations | Supporting Information

ABSTRACT: The design and discovery of three-dimensional crystalline metal–organic frameworks (MOFs) from linkers with phosphonate coordinating groups and even alkaline earth metals is largely undeveloped. Herein, we report a strategy for realizing new, stable, and robust barium phosphonate MOFs, termed Empa-1 and Empa-2. The two-dimensional (2D) Empa-1 or three-dimensional (3D) Empa-2 could be realized by way of systematically modulating the ratio of Ba^{2+} with a tetratopic phosphonate-based linker that was crafted to incorporate nitrogen-rich triazine units bridged by a fixed piperazine core. In addition to this synthetic approach, temperature-dependent synchrotron-radiation powder X-ray diffraction analysis demonstrated that the 2D Empa-1 undergoes an irreversible phase transition upon heating and subsequent dehydration to form the 3D Empa-2. Given the presence of uncoordinated phosphonic acid moieties within the structure of 3D Empa-2, the CO_2 sorption capabilities are reported. We believe our ability to link the alkaline earth metal barium with a novel tetratopic phosphonate linker, as evidenced by the robust structures of Empa-1 and -2, paves the way for further exploration and discovery of new crystalline, porous frameworks with greater structural diversity, stability, and wide-scale practical applicability.

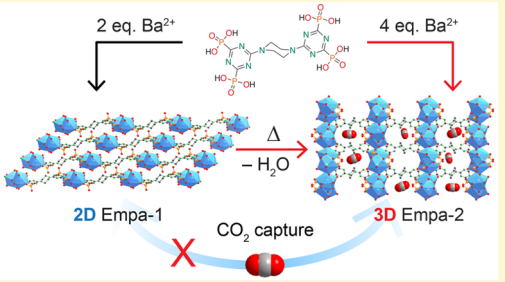

In the continued quest to design and discover new metal–organic frameworks (MOFs), linkers with multichelating phosphonate groups are viewed as promising alternatives to the traditionally employed organic linkers based on carboxylate coordinating groups.[1−3] Given the hard character of the phosphonate oxygen atoms, these linkers are attractive because they provide synthetic access to a number of thermally and chemically stable MOFs when using hard metal ions.[4−7] The challenge with employing phosphonate-based linkers in the construction of new MOFs is their propensity to react quickly, which greatly increases the difficulty in retaining control over the growth of large single crystals that are needed for structural elucidation and analysis.[8−10] This is a critical aspect to overcome as the coordination chemistry of phosphonate groups is markedly less predictable than that of carboxylate coordinating groups.[2] Furthermore, phosphonate-based linkers have a notable tendency to yield dense-layered MOF structures, thereby limiting their scope of application.[2] However, this can be overcome by introducing a fixed, bridging organic core between the phosphonate coordinating groups to facilitate the formation of an open framework.[2]

In this contribution, we report a synthetic approach for realizing two new phosphonate-based MOFs, termed Empa-1 and Empa-2, using a nitrogen enriched phosphonate-based linker and Ba^{2+} as the metal ion. It is important to note that these two structures significantly expand the small library of known MOFs constructed from phosphonate-based linkers and alkaline-earth metal ions.[11−17] Our design strategy for realizing Empa-1 and -2 was predicated on the systematic modulation of the Ba^{2+} to phosphonate-based linker molar ratio. Single-crystal X-ray diffraction structural analysis confirmed that Empa-1 adopted a two-dimensional (2D) layered structure as a result of reacting Ba^{2+} to the phosphonate-based linker in a molar ratio of 2:1. With Empa-1 in hand, we discovered two routes for realizing the

Received: May 7, 2021
Accepted: June 10, 2021

https://doi.org/10.1021/acsmaterialslett.1c00275
ACS Materials Lett. 2021, 3, 1010–1015

three-dimensional (3D), open framework of Empa-2. The first was through a prescribed Ba^{2+} to phosphonate-based linker ratio of 4:1 or higher during the synthesis regardless of the other conditions employed. In addition to this synthetic approach, we found through temperature-dependent synchrotron powder X-ray diffraction analysis measurements that the 2D Empa-1 undergoes an irreversible phase transition via water loss to form the 3D Empa-2. Given its open framework and the presence of uncoordinated phosphonic acid moieties, Empa-2 displays CO_2 sorption capabilities marked by a relatively high enthalpy of CO_2 adsorption. The CO_2 sorption affinity of Empa-2 was further investigated using attenuated total reflectance infrared spectroscopy combined with an integrated quantum mechanics−molecular mechanics computational method to provide deeper insight into the adsorption process.

The designed tetratopic phosphonate-based linker, piperazine-1,4-diylbis(1,3,5-triazine-6,2,4-triyl))tetrakis(phosphonic acid) (H_8-PTT), was synthesized in a process comprised of three-steps:[18] (i) Michaelis−Arbuzov rearrangement of cyanuric chloride with triethyl phosphite; (ii) nucleophilic substitution on the triazine carbon with piperazine; and finally, (iii) McKenna reaction to produce the targeted phosphonic acid (see Supporting Information, section S1). Crystals of Empa-1 were obtained in a yield of 89% by adding an aqueous solution of $BaBr_2{\cdot}2H_2O$ to an aqueous solution of H_8-PTT at room temperature in a 2:1 Ba^{2+} to H_8-PTT molar ratio (Figure 1). We note that the alkaline earth metal barium was chosen because of its large size to charge ratio, as well as its coordinative pliancy (SI, section S1).[15]

Single crystal X-ray diffraction (XRD) analysis revealed that Empa-1 crystallizes in the triclinic space group $P\bar{1}$ (No. 2) with lattice parameters a = 7.42689(10) Å, b = 8.53905(15) Å, c = 13.3756(2) Å, α = 82.1589(14)°, β = 76.4697(13)°, and γ = 88.4765(12)° (SI, Table S1). The 2D layered structure of Empa-1 is highlighted by the partial deprotonation of H_8-PTT to H_4-PTT resulting in a 4^- overall charge. The H_4-PTT linker coordinates to four Ba^{2+} centers via two 1.100 monodentate and two 2.200 bidentate phosphonate groups (Harris notation) and two nitrogen atoms from triazine (Figure 1).[19] For its part, barium forms an infinite one-dimensional rod of edge-sharing, capped square antiprismatic $\{BaO_8N\}$ units with each barium adopting a coordination number of 9 from three H_4-PTT oxygen atoms, three terminal and two bridging water molecules and one nitrogen atom. Within each layer, the P═O double bonds of the H_4-PTT linker are aligned above and below their corresponding layer planes and are involved in intermolecular H-bonds with P−OH groups. These intermolecular interactions are attributable to the displacement of the framework layers, which precluded the formation of 2D infinite rod building units of barium. The Ba−O (H_4-PTT) and Ba−O (H_2O) bond lengths vary in the range of 2.7548(7)−2.8017(7) and 2.7270(9)−2.9771(8) Å, respectively, and the Ba−N (triazine) bond length is 2.9566 (8) Å (SI, Table S2). Finally, the Ba−Ba distances in the edge-sharing, capped square antiprismatic $\{BaO_8N\}$ units of the 1D infinite rod are in the range of 4.5571(2) to 5.0657(3) Å and the Ba−Ba distances between layers are 7.4269(2) Å.

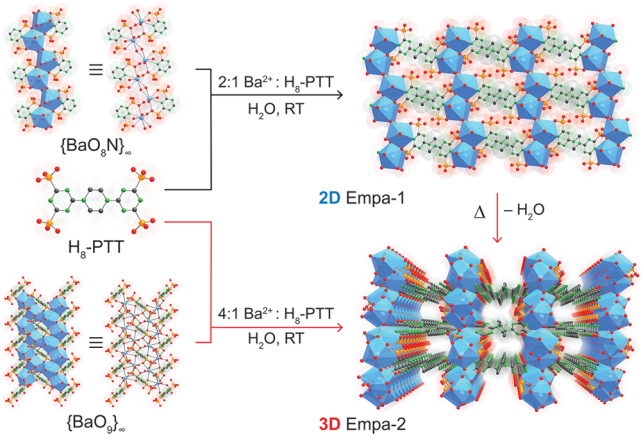

Figure 1. Crystal structure of the two-dimensional (2D) Empa-1 (top) and the three-dimensional (3D) Empa-2 (bottom). Empa-1 was constructed from infinite one-dimensional rods of edge-sharing, capped square antiprismatic $\{BaO_8N\}$ units that are stitched together by the tetratopic phosphonate-based linker, (piperazine-1,4-diylbis(1,3,5-triazine-6,2,4-triyl))tetrakis-(hydrogen phosphonate) (H_4-PTT). Empa-2 is synthesized from infinite quasi-hexagonal layers of face- and edge-sharing $\{BaO_9\}$ polyhedra that are connected by the H_4−PTT linkers. The 3D Empa-2 can be realized by modulating the Ba^{2+} to H_8−PTT molar ratio or by dehydrating Empa-1. Atom colors: Ba, blue polyhedral; C, gray; O, red; P, orange; and N, green. H atoms are omitted for clarity.

A combination of thermal gravimetric (TGA) and elemental analyses (EA) were utilized to uncover a plausible chemical formula for Empa-1. The TGA curve displayed a two-step dehydration process with a weight percent loss of 12% from 25 to ∼80 °C and 4% from ∼80 to 140 °C, which corresponds to loss of occluded lattice water molecules and partial loss of coordinated water ligands, respectively (SI, Figure S7). EA was then performed using a sample that was dried at ambient temperature overnight resulting in 11.79%, 3.16%, and 10.88%, for C, H, and N, respectively, being found. From these two techniques, the chemical formula of Empa-1 is concluded to be $Ba_2(H_4\text{-PTT}){\cdot}12H_2O$.

Over the course of handling and characterizing Empa-1, we began to observe changes to the sample as a function of time. Therefore, the structural integrity of Empa-1 was investigated by temperature-dependent synchrotron-radiation powder XRD. The resulting obtained PXRD patterns were refined by optimizing peak profiles, zero shift, background, asymmetry, and unit cell parameters at ambient temperature. As shown in Figure 2, the PXRD pattern at ambient temperature indicated that we were correct in that Empa-1 was present with a second, previously unknown, phase. This confirms that Empa-1 undertakes a slow phase transition even under long-term ambient conditions. The phase transition process was confirmed upon heating Empa-1 to temperatures >90 °C as evidenced by a noticeable change in the diffraction pattern from the initial two-phase mixture to a pure unknown phase. We note that the observations made in the TGA experiments are consistent with those found in the temperature-dependent XRD experiment. Specifically, the loss of occluded lattice water molecules (12 wt %) from ambient temperature to ca. 80 °C is consistent with the phase transition while at the same time the partial loss of coordinated water ligands (4 wt %) between 80 and 140 °C correlates to the completion of the phase transition (Figure 2 and SI, sections S3 and S4). Indexing and, subsequent, Pawley refinement on this end diffraction pattern resulted in a polymorph that crystallized in the monoclinic space group $P2_1/c$ (No. 14) with lattice parameters of a = 14.1218(1) Å, b = 13.4637(1) Å, and c = 7.0544(1) Å, $\alpha = \gamma$ = 90° and β = 105.25(1)° (SI, section S4).

https://doi.org/10.1021/acsmaterialslett.1c00275
ACS Materials Lett. 2021, 3, 1010−1015

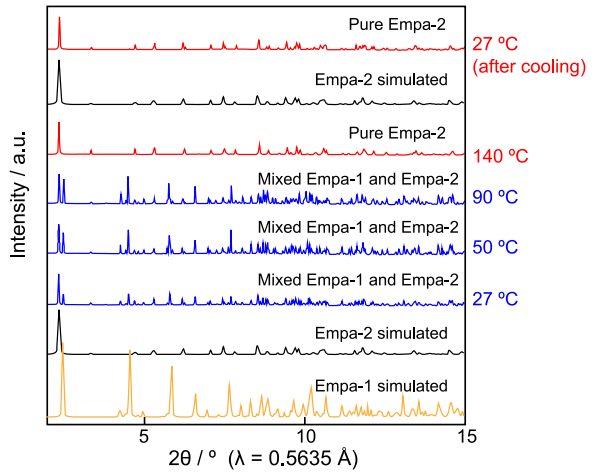

Figure 2. Synchrotron-radiation powder X-ray diffraction measurements collected at different temperatures. At ambient temperature (27 °C), there is a mixture of two polymorphs (blue patterns). The mixture remains as the temperature increases from 50 to 90 °C (blue patterns). At 140 °C, there is a complete phase transition from Empa-1 to Empa-2 (red pattern). The pure Empa-2 polymorph remains even after the sample is cooled back down to 27 °C (red pattern). The theoretical diffraction patterns calculated from the single-crystal structures of Empa-1 (yellow pattern) and Empa-2 (black pattern) are provided as a reference.

Different strategies were explored to understand whether the more stable polymorph could be isolated synthetically. By following the same synthetic recipe as Empa-1, albeit with an increased 4:1 Ba^{2+} to H_8-PTT molar ratio (or higher), the more stable monoclinic polymorph, now termed Empa-2, could be synthetically isolated in 72% yield. From single-crystal XRD analysis, the structure of Empa-2 was solved in the monoclinic space group $P2_1/c$ (No. 14) with lattice parameters a = 14.0869(11) Å, b = 13.5308(10) Å, c = 7.0893(5) Å, $\alpha = \gamma$ = 90°, and β = 104.185(6)° (SI, Table S1). Not only did powder XRD analysis reveal only one pure phase for the synthetically produced Empa-2 but also a diffraction pattern and lattice parameters that were in high coincidence with the end powder XRD pattern obtained from the temperature-dependent measurements.

In contrast, Empa-2 adopts a 3D structure characterized by 1D open, rectangular channels (~5 × 7.6 Å) along its c axis (Figure 1). Similar to the 2D polymorph, the structure of Empa-2 is highlighted by a partial deprotonation of H_8-PTT to H_4-PTT resulting in a 4^- overall charge on the linker. However, in Empa-2, the H_4-PTT linker coordinates to 12 Ba^{2+} centers via two 4.222 hexadentate and two 2.200 bidentate phosphonate groups (Harris notation), resulting in Ba^{2+} polyhedra with tricapped trigonal prismatic geometry. The final coordination site (coordination number for Ba^{2+} in Empa-2 = 9) is occupied by one water ligand. Each Ba^{2+} polyhedra has two face-sharing sides and one edge-sharing side with Ba−Ba distances of 4.3636(4) and 4.5016(5) Å, respectively (SI, Figure S6). This produces infinite quasi-hexagonal layers of $\{BaO_9\}$ polyhedra (Figures 1 and S6). The formation of this infinite quasi-hexagonal layer is controlled by the adjacent phosphonate groups on the same linker, in which one phosphonate group coordinates to four different Ba^{2+} centers (4.222 coordination mode) and the other coordinates to two different Ba^{2+} centers (2.200 coordination mode).[19] Each quasi-hexagonal six membered group of $\{BaO_9\}$ polyhedra is supported by two H_4-PTT linkers, so that two of each of the phosphonate groups with similar coordination modes coordinate antiparallel with respect to each other.

After formation, Empa-2 avoids collapse or further structural transformation due to the coordination mode of the H_4-PTT linker's phosphonate groups that serve to lock the positions and directions of the Ba^{2+} centers into the infinite rigid quasi-hexagonal groups of $\{BaO_9\}$ polyhedra. Further structural reinforcement is provided by intermolecular H-bonding that is created by adjacent phosphonate groups (P═O···H−O−P distance = 1.751(3) Å). A linker-based interlayer was found occupying the center of the quasi-hexagonal $\{BaO_9\}$ polyhedra, which arranges in a zigzag structure to produce additional channels in zigzag form. The combination of the channels along the c axis with these zigzag channels that proliferate along the a axis result in a 3D open framework.

Similar to the case of Empa-1, a combination of TGA and EA were utilized to define the chemical formula of Empa-2. The TGA curve exhibited a weight loss of 4.5% up to 65 °C and 3.3% up to 170 °C that was attributed to the loss of occluded lattice water molecules and partial loss of coordinate water ligands, respectively (SI, section S3). EA was then performed on a dried sample of Empa-2, which found 12.94%, 2.17%, and 12.11%, for C, H, and N, respectively. With the results taken together, the same chemical formula of $Ba_2(H_4\text{-PTT})\cdot 4H_2O$ was concluded for Empa-2.

To better understand the phase transition and structural relationship between Empa-1 and Empa-2, density functional theory calculations were performed (SI, section S5).[20,21] Accordingly, the completely relaxed PBE-D3(BJ) structures of Empa-1 and Empa-2 were in satisfactory agreement with the experimentally derived crystals structures given that both the computationally derived lattice parameters and unit cell volumes were within ~2% of the corresponding experimental values. It is noted that the total energies of the two structures cannot be compared directly due to difference in water content of the refined structures. Thus, we calculated the reaction energy following:

$$\text{Empa-1}_{uc} \rightarrow 1/2\text{Empa-2}_{uc} + 8H_2O$$

where Empa-1_{uc} and Empa-2_{uc} refer to the unit cells of the crystals (Z = 1 and Z = 2, respectively) including the lattice water molecules. At the PBE-D3(BJ) level, the calculated energy for the transformation from Empa-1 to Empa-2 was found to be 6.67 eV per formula unit. That is, Empa-1 was calculated to be significantly more stable than Empa-2 at low temperatures. Both crystal structures contain four occluded lattice water molecules in their unit cells. The energy of the transformation from Empa-1 to Empa-2 after the occluded lattice water had been removed from each was found to be smaller at 4.53 eV per formula unit. This indicates that the occluded lattice water molecules stabilize the higher energy Empa-2 more so than Empa-1. Nonetheless, regardless of whether the occluded lattice water molecules are removed, the 2D Empa-1 structure remains slightly lower in energy than the 3D Empa-2 structure. Attempts to predict the temperature-dependent relative stability between Empa-1 and Empa-2 via phonon calculations failed. Such detailed calculations revealed the Empa-2 crystal possesses soft modes associated with vibrations of the strained piperazine linkages, which makes attempts to analyze the calculated free energy differences between the two polymorphs unreliable.

https://doi.org/10.1021/acsmaterialslett.1c00275
ACS Materials Lett. 2021, 3, 1010−1015

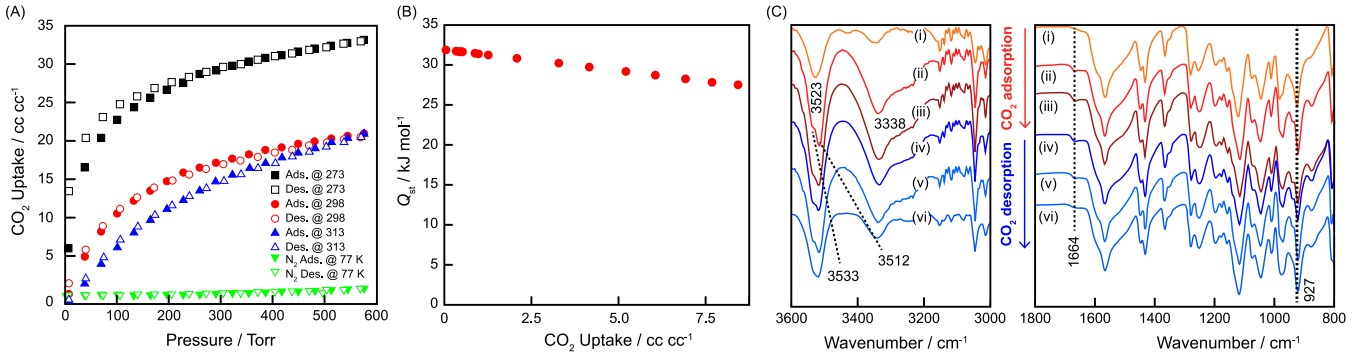

Figure 3. (A) CO_2 adsorption isotherms at 273 (black squares), 298 (red circles), and 313 K (blue triangles) for Empa-2. N_2 adsorption isotherm at 77 K (green triangles) is also presented. Closed and open symbols represent the adsorption and desorption branches, respectively. (B) Coverage-dependent isosteric enthalpy of adsorption (Q_{st}) calculated from the CO_2 isotherms measured at 273, 298, and 313 K. (C) Attenuated total reflectance infrared (ATR-IR) spectra of (i) activated Empa-2, (ii) Empa-2 exposed to CO_2 at ambient conditions for 2 h, (iii) Empa-2 exposed to CO_2 at ambient conditions for 16 h, and the ATR-IR spectra of Empa-2 after CO_2 desorption at 75 °C for (iv) 1, (v) 2, and (vi) 4 h.

Given its 1D open rectangular channels, we then sought to assess the porosity of Empa-2. The N_2 isotherm at 77 K was measured after solvent exchange and activation at 100 °C under reduced pressure (1.0×10^{-2} mbar) for 12 h. Surprisingly, Empa-2 did not adsorb any N_2 at 77 K and, therefore, a Brunauer–Emmett–Teller surface area was not calculated (Figure 3A). Speculating that adsorbate size or N_2-phobicity could play as factors for this, we turned our attention to measuring the thermodynamic CO_2 uptake at 273, 298, and 313 K (SI, section S6).[22] At 273 K, the volumetric CO_2 uptake capacity saturated at a moderate value of ~33 cc cc^{-1}. However, it was noted that the initial adsorption slopes at low pressures (<80 Torr) were considerably steep with the majority of the volumetric uptake occurring in this region (SI, Figure S11). This indicated strong interactions were arising between CO_2 and Empa-2, which was to be expected given the presence of uncoordinated phosphonic acid moieties. Coverage-dependent isosteric enthalpy of adsorption (Q_{st}) was calculated using a virial-type expansion equation applied to the data collected from the CO_2 isotherms measured at three temperatures (Figure 3B). At zero-coverage, the Q_{st} was found to be ~32 kJ mol^{-1}— a value that provides a quantifiable explanation for the strong interactions between CO_2 and Empa-2 occurring at low pressures.

The mechanism of CO_2 adsorption within Empa-2 was studied via attenuated total reflectance infrared (ATR-IR) spectroscopy measurements (Figure 3C). For this, Empa-2 was exposed to CO_2 at ambient conditions for 2 h, which resulted in characteristic changes in its ATR-IR spectrum with respect to the spectrum obtained for a blank sample. Specifically, upon adsorption, the broad absorption band at ~3523 cm^{-1} split into two distinct bands centered at 3533 and 3512 cm^{-1}, respectively. This splitting occurs as a result of CO_2 perturbation upon insertion into the PO···H–OP hydrogen bond. From density functional theory (DFT) calculations, the O–H bond length becomes 0.039 Å shorter than the unperturbed ones (SI, section S5 and Figure S10). For this potential, the calculated value of the vibrational frequency of the PO–H stretching mode (3514 cm^{-1}) is in remarkably good agreement with experimental results. A new absorption band appeared at 3338 cm^{-1} (theoretically, 3348 cm^{-1}) as a result of the existence of new intermolecular interactions arising from CO_2 and PO–H. The two characteristic bands of the phosphonate linker's 1,3,5-triazine units, centered at 1664 and 927 cm^{-1}, shifted to wavenumbers, 1515 and 939 cm^{-1}, respectively, upon the adsorption CO_2. Increasing the exposure time of Empa-2 to CO_2 from 2 to 16 h, did not influence the absorption band intensities, which revealed that the sample becomes quickly saturated with CO_2. When the CO_2-exposed Empa-2 was heated to 75 °C, the ATR-IR spectra displayed a gradual decrease in absorption band intensities as a function of time. Consequently, the captured CO_2 can be reversibly released from the pores (Figure 3C).

In summary, we have synthesized and fully characterized two new phosphonate-based MOFs. In particular, Empa-2 is (i) formed by either direct synthesis (i.e., increasing the Ba^{2+} ratio to phosphonate linker) or through dehydration of the 2D phosphonate-based MOF, Empa-1, upon heating, (ii) replete with uncoordinated phosphonic acid moieties that line the rectangular channels of the MOF, (iii) capable of reversibly adsorbing CO_2 by way of its uncoordinated phosphonic acid moieties, and (iv) demonstrated to have a heat of adsorption value that is appropriate for strong, yet regenerable binding of CO_2.

■ ASSOCIATED CONTENT

Supporting Information

The Supporting Information is available free of charge at https://pubs.acs.org/doi/10.1021/acsmaterialslett.1c00275.

Synthesis and full characterization details of Empa-1 and Empa-2, including data pertaining to single crystal X-ray diffraction, powder X-ray diffraction, thermal gravimetric, elemental, gas sorption, and computational modeling analyses (PDF)

Single-crystal structure of Empa-1 (CCDC 2043102) (CIF)

Single-crystal structure of Empa-2 (CCDC 2043101) (CIF)

■ AUTHOR INFORMATION

Corresponding Authors

Khalifah A. Salmeia – *Department of Chemistry, Faculty of Science, Al-Balqa Applied University, 19117 Al-Salt, Jordan; Laboratory for Advanced Fibers, Empa, Swiss Federal Laboratories for Materials Science and Technology, St. Gallen, Switzerland;* orcid.org/0000-0003-2541-9652; Email: khalifah.salmeia@bau.edu.jo

https://doi.org/10.1021/acsmaterialslett.1c00275
ACS Materials Lett. 2021, 3, 1010–1015

Antonia Neels − *Center for X-ray Analytics, Empa, Swiss Federal Laboratories for Materials Science and Technology, 8600 Dübendorf, Switzerland; Department of Chemistry, University of Fribourg, 1700 Fribourg, Switzerland;* orcid.org/0000-0001-5752-2852; Email: antonia.neels@empa.ch

Authors

Simone Dolabella − *Center for X-ray Analytics, Empa, Swiss Federal Laboratories for Materials Science and Technology, 8600 Dübendorf, Switzerland; Department of Chemistry, University of Fribourg, 1700 Fribourg, Switzerland*

Dambarudhar Parida − *Laboratory for Advanced Fibers, Empa, Swiss Federal Laboratories for Materials Science and Technology, St. Gallen, Switzerland*

Terry J. Frankcombe − *School of Science, University of New South Wales, 2610 Canberra BC, Australian Capital Territory, Australia;* orcid.org/0000-0001-9791-5394

Akef T. Afaneh − *Department of Chemistry, Faculty of Science, Al-Balqa Applied University, 19117 Al-Salt, Jordan;* orcid.org/0000-0001-8353-9578

Kyle E. Cordova − *Materials Discovery Research Unit, Advanced Research Centre, Royal Scientific Society, 11941 Amman, Jordan;* orcid.org/0000-0002-4988-0497

Bassem Al-Maythalony − *Materials Discovery Research Unit, Advanced Research Centre, Royal Scientific Society, 11941 Amman, Jordan*

Shanyu Zhao − *Laboratory for Building Energy Materials and Components, Empa, Swiss Federal Laboratories for Materials Science and Technology, 8600 Dübendorf, Switzerland;* orcid.org/0000-0002-8863-7019

Romain Civioc − *Laboratory for Building Energy Materials and Components, Empa, Swiss Federal Laboratories for Materials Science and Technology, 8600 Dübendorf, Switzerland*

Ali Marashdeh − *Department of Chemistry, Faculty of Science, Al-Balqa Applied University, 19117 Al-Salt, Jordan*

Bernhard Spingler − *Department of Chemistry, University of Zurich, 8057 Zurich, Switzerland;* orcid.org/0000-0003-3402-2016

Ruggero Frison − *Center for X-ray Analytics, Empa, Swiss Federal Laboratories for Materials Science and Technology, 8600 Dübendorf, Switzerland*

Complete contact information is available at: https://pubs.acs.org/10.1021/acsmaterialslett.1c00275

Author Contributions

‡S.D. and D.P. contributed equally to this work. The manuscript was written through contributions of all authors. All authors approved the final version of the manuscript.

Notes

The authors declare no competing financial interest.

■ ACKNOWLEDGMENTS

S.D. is grateful to the Swiss National Science Foundation (Grant 169257) for the financial support of this work. The NMR measurements were partially granted by the Swiss National Science Foundation (Grant 150638). The Synergy diffractometer was purchased with partial support by the R'Equip program of the Swiss National Science Foundation (Project No. 206021_164018). This research was undertaken with the assistance of resources and services from the National Computational Infrastructure, which is supported by the Australian Government. B.A.M. and K.E.C. acknowledge financial support from the Alliance of International Science Organizations (ANSO; No. ANSO-CR-PP-2020-06) for CO_2 adsorption measurements. K.E.C. acknowledges the Synchrotron-light for Experimental Science and Applications in the Middle East (SESAME; MS Beamline No. 20190028) for beamtime and Dr. Mahmoud Abdellatief (MS Principal Beamline Scientist) for his support with temperature-dependent measurements. B.A.M is grateful to Ms. Ala'a Al-Ghourani, Ms. Aya Khreis, and Ms. Rada Abaza (Royal Scientific Society) for technical support and data processing.

■ REFERENCES

(1) Yücesan, G.; Zorlu, Y.; Stricker, M.; Beckmann, J. Metal-Organic Solids Derived from Arylphosphonic Acids. *Coord. Chem. Rev.* **2018**, *369*, 105−122.

(2) Gagnon, K. J.; Perry, H. P.; Clearfield, A. Conventional and Unconventional Metal-Organic Frameworks Based on Phosphonate Ligands: MOFs and UMOFs. *Chem. Rev.* **2012**, *112*, 1034−1054.

(3) Bhanja, P.; Na, J.; Jing, T.; Lin, J.; Wakihara, T.; Bhaumik, A.; Yamauchi, Y. Nanoarchitectured Metal Phosphates and Phosphonates: A Material Horizon toward Emerging Applications. *Chem. Mater.* **2019**, *31*, 5343−5362.

(4) Tholen, P.; Zorlu, Y.; Beckmann, J.; Yücesan, G. Probing Isoreticular Expansions in Phosphonate MOFs and Their Applications. *Eur. J. Inorg. Chem.* **2020**, *2020*, 1542−1554.

(5) Chen, X.; Peng, Y.; Han, X.; Liu, Y.; Lin, X.; Cui, Y. Sixteen Isostructural Phosphonate Metal-Organic Frameworks with Controlled Lewis Acidity and Chemical Stability for Asymmetric Catalysis. *Nat. Commun.* **2017**, *8*, 2171.

(6) Taylor, J. M.; Dawson, K. W.; Shimizu, G. K. H. A Water-Stable Metal-Organic Framework with Highly Acidic Pores for Proton-Conducting Applications. *J. Am. Chem. Soc.* **2013**, *135*, 1193−1196.

(7) Maares, M.; Ayhan, M. M.; Yu, K. B.; Yazaydin, A. O.; Harmandar, K.; Haase, H.; Beckmann, J.; Zorlu, Y.; Yücesan, G. Alkali Phosphonate Metal-Organic Frameworks. *Chem. - Eur. J.* **2019**, *25*, 11214−11217.

(8) Shimizu, G. K. H.; Vaidhyanathan, R.; Taylor, J. M. Phosphonate and Sulfonate Metal Organic Frameworks. *Chem. Soc. Rev.* **2009**, *38*, 1430−1449.

(9) Zheng, T.; Yang, Z.; Gui, D.; Liu, Z.; Wang, X.; Dai, X.; Liu, S.; Zhang, L.; Gao, Y.; Chen, L.; Sheng, D.; Wang, Y.; Diwu, J.; Wang, J.; Zhou, R.; Chai, Z.; Albrecht-Schmitt, T. E.; Wang, S. Overcoming the Crystallization and Designability Issues in the Ultrastable Zirconium Phosphonate Framework System. *Nat. Commun.* **2017**, *8*, 15369.

(10) Wang, Y.; Wang, X.; Huang, Y.; Zhou, F.; Qi, C.; Zheng, T.; Li, J.; Chai, Z.; Wang, S. Reticular Chemistry of Uranyl Phosphonates: Sterically Hindered Phosphonate Ligand Method is Significant for Constructing Zero-Dimensional Secondary Building Units. *Chem. - Eur. J.* **2019**, *25*, 12567−12575.

(11) Colodrero, R. M. P.; Olivera-Pastor, P.; Losilla, E. R.; Hernández-Alonso, D.; Aranda, M. A. G.; Leon-Reina, L.; Rius, J.; Demadis, K. D.; Moreau, B.; Villemin, D.; Palomino, M.; Rey, F.; Cabeza, A. High Proton Conductivity in a Flexible, Cross-Linked, Ultramicroporous Magnesium Tetraphosphonate Hybrid Framework. *Inorg. Chem.* **2012**, *51*, 7689−7698.

(12) Ramaswamy, P.; Wong, N. E.; Gelfand, B. S.; Shimizu, G. K. H. A Water Stable Magnesium MOF That Conducts Protons over 10^{-2} S cm^{-1}. *J. Am. Chem. Soc.* **2015**, *137*, 7640−7643.

(13) Fard, Z. H.; Kalinovskyy, Y.; Spasyuk, D. M.; Blight, B. A.; Shimizu, G. K. H. Alkaline-Earth Phosphonate MOFs with Reversible Hydration-Dependent Fluorescence. *Chem. Commun.* **2016**, *52*, 12865−12868.

(14) Taylor, J. M.; Vaidhyanathan, R.; Iremonger, S. S.; Shimizu, G. K. H. Enhancing Water Stability of Metal-Organic Frameworks via Phosphonate Monoester Linkers. *J. Am. Chem. Soc.* **2012**, *134*, 14338−14340.

(15) Gelfand, B. S.; Taylor, J. M.; Shimizu, G. K. H. Extracting Structural Trends from Systematic Variation of Phosphonate/Phosphonate Monoester Coordination Polymers. *CrystEngComm* **2017**, *19*, 3727−3736.
(16) Vaidhyanathan, R.; Mahmoudkhani, A. H.; Shimizu, G. K. H. A Microporous Alkaline-Earth Phosphonate Sustained by One-Dimensional Inorganic and Organic Units. *Can. J. Chem.* **2009**, *87*, 247−253.
(17) Bazaga-García, M.; Colodrero, R. M. P.; Papadaki, M.; Garczarek, P.; Zoń, J.; Olivera-Pastor, P.; Losilla, E. R.; León-Reina, L.; Aranda, M. A. G.; Choquesillo-Lazarte, D.; Demadis, K. D.; Cabeza, A. Guest Molecule-Responsive Functional Calcium Phosphonate Frameworks for Tuned Proton Conductivity. *J. Am. Chem. Soc.* **2014**, *136*, 5731−5739.
(18) Salmeia, K. A.; Neels, A.; Parida, D.; Lehner, S.; Rentsch, D.; Gaan, S. Insight into the Synthesis and Characterization of Organophosphorus-Based Bridged Triazine Compounds. *Molecules* **2019**, *24*, 2672.
(19) Coxall, R. A.; Harris, S. G.; Henderson, D. K.; Parsons, S.; Tasker, P. A.; Winpenny, R. E. P. Inter-Ligand Reactions: In Situ Formation of New Polydentate Ligands. *Dalton Trans.* **2000**, *14*, 2349−2356.
(20) Kresse, G.; Joubert, D. From Ultrasoft Pseudopotentials to the Projector Augmented-Wave Method. *Phys. Rev. B: Condens. Matter Mater. Phys.* **1999**, *59*, 1758−1775.
(21) Kresse, G.; Furthmüller, J. Efficiency of Ab-Initio Total Energy Calculations for Metals and Semiconductors Using a Plane-Wave Basis Set. *Comput. Mater. Sci.* **1996**, *6*, 15−50.
(22) Patel, H. A.; Je, S. H.; Park, J.; Chen, D. P.; Jung, Y.; Yavuz, C. T.; Coskun, A. Unprecedented High-Temperature CO_2 Selectivity in N_2-Phobic Nanoporous Covalent Organic Polymers. *Nat. Commun.* **2013**, *4*, 1357.

https://doi.org/10.1021/acsmaterialslett.1c00275
ACS Materials Lett. 2021, 3, 1010−1015